Soil Dynamics and Earthquake Engineering 95 (2017) 153–166

Contents lists available at ScienceDirect

Soil Dynamics and Earthquake Engineering

journal homepage: www.elsevier.com/locate/soildyn

On the spatial variability of CPT-based geotechnical parameters for regional liquefaction evaluation

Chaofeng Wang, Qiushi Chen*, Mengfen Shen, C. Hsein Juang

Glenn Department of Civil Engineering, Clemson University, Clemson, SC 29634, United States

ARTICLE INFO

Keywords:
Liquefaction
Cone penetration test
Random field
Spatial variability
Liquefaction potential index

ABSTRACT

In-situ index tests, such as the cone penetration test (CPT), are widely used for the site-specific evaluation of liquefaction potential and are getting increased use in the regional mapping of liquefaction hazards. In this work, the spatial variability of CPT-based geotechnical parameters on the liquefaction potential evaluation is assessed through an integrated framework combining an empirical liquefaction model and a multiscale random field model that allows the effective incorporation of soil spatial variability across scales. Within this framework, two approaches, termed the local soil property approach and the averaged index approach, are developed and assessed for the characterization of spatial variability in CPT-based geotechnical parameters. The proposed framework is applied to the probabilistic and spatial assessment of the liquefaction potential of an earthquake-prone region to demonstrate its applicability and to investigate the implications of spatial variability on regional liquefaction susceptibility evaluation.

1. Introduction

Earthquake-induced liquefaction of soils often causes significant damage to infrastructure such as buildings, bridges, and lifelines [1]. Evaluating the likelihood of liquefaction and the associated geohazards involve analysis of ground shaking hazard and liquefaction susceptibility of the soil deposit [2]. In practice, the use of the empirical correlations of the observed field behavior with various in-situ index tests, such as the Cone Penetration Test (CPT), the Standard Penetration Test (SPT) and the shear wave velocity test, remains the dominating approach for assessing liquefaction potential; see [3] for a summary and recommendation of various in-situ test-based liquefaction models. Building on the empirical models, the direct output of a liquefaction evaluation procedure is typically expressed in terms of factor of safety against liquefaction triggering in a soil stratum at depth. The damage potential of liquefaction can then be linked to the factor of safety through a nonlinear depth integration such as the liquefaction potential index (LPI) proposed in [4].

The empirical models evaluate the liquefaction potential at individual locations where field tests are performed. Estimation of liquefaction potential at locations away from the measurement site requires some degrees of spatial continuity of soil properties. In other words, soil properties, as indicated by the representative indices like the tip resistance q_c and the side friction f_s from CPT measurements, are spatially correlated [5]. Tools in geostatistics [6,7] have been used to model such spatial variation of soil properties as a random field. Interpolation and stochastic simulation techniques are then used to estimate the spatial distribution of properties at a site. In the context of liquefaction analysis, examples of work along this line include [8–17].

To account for the spatial variability of geotechnical properties in the liquefaction evaluation procedure, two approaches will be developed and assessed in this work. The first approach, termed *the local soil property approach*, treats the local field data (e.g., the CPT tip resistance and side friction) as spatially correlated soil properties across the region. Random fields of field data are realized in a layer-by-layer sequence, i.e., only the horizontal correlation is explicitly modeled. Examples of existing efforts along this line include [18,19,12,14,16]. On a smaller scale, e.g., a specimen in the lab or for a relatively small area around a field bore-hole location, full three-dimensional random field models have also been proposed to characterize spatially correlated soil properties and applied to liquefaction evaluation [9–11]. However, generating full three-dimensional random field models on a regional scale not only poses increased computational challenge but may not guarantee a more accurate result in liquefaction evaluation since now both vertical and horizontal correlations need to be simultaneously accounted for using available field data. The scales of variations in the vertical and horizontal directions can be different in order of magnitude over a region (e.g., centimeter in the vertical direction vs. meter or kilometer in the horizontal direction). For these reasons, a more sophisticated three-dimensional random field model

* Corresponding author.
E-mail address: qiushi@clemson.edu (Q. Chen).

http://dx.doi.org/10.1016/j.soildyn.2017.02.001
Received 25 March 2016; Received in revised form 2 December 2016; Accepted 1 February 2017

may not yield better estimation therefore will not be considered here.

An alternative approach, termed *the averaged index approach*, computes an averaged soil property or index (e.g., the liquefaction potential index or liquefaction probability) at individual locations where field data are available. Then, interpolations or geostatistical tools and random field models are utilized to generate the averaged index properties at unmeasured or unsampled locations across the region. This approach is much more commonly used in liquefaction mapping over extended area, e.g., [20–24,13,17], since it only requires characterization and/or random field realizations of an averaged quantity of interest, i.e., the liquefaction potential index, in the horizontal direction. This makes parameter identification more straightforward and is much more computationally efficient when evaluating liquefaction susceptibility over large areas. However, by calculating an averaged index, details of soil properties are no long available for the region and the effect of this averaging process on the estimated liquefaction potential is unknown.

While both approaches have been applied to evaluate liquefaction potential across a region, the implications of these two approaches on the liquefaction risk have yet to be addressed. Moreover, much existing experience with random field models for soil properties is limited to a single spatial scale. When evaluating liquefaction potential over an extended region, spatial variability of geotechnical parameters often manifests at different scales, i.e., boring data (local scale) vs. surficial geological features (regional scale). Field data are oftentimes sparse and the uncertainties away from local boring data can be large. A multiscale consideration is deemed necessary. In this work, a multiscale random field model [25,26,17] will be integrated with empirical liquefaction models for the evaluation of liquefaction potential over extended areas.

We will assess how *the local soil property* and *the averaged index property* approaches affect the evaluation of liquefaction potential in spatially variable soils. The proposed framework is among the first efforts to integrate multiscale local soil property and averaged index random fields with liquefaction potential evaluation. The applicability and assessment of these random fields will be demonstrated through the probabilistic and spatial assessment of liquefaction potential in a liquefaction-prone region.

2. General framework

In this work, the CPT-based empirical liquefaction model is integrated with geostatistical tools to account for the spatial variability of geotechnical properties for regional liquefaction evaluation. The flow of the general framework to account for spatial variability is shown in Fig. 1. As shown in Fig. 1, within a liquefaction-prone region, CPT measurements (e.g., the tip resistance and the side friction) and other geotechnical data of interest (e.g., water table, soil unit weight, etc.) are first collected and their geostatistical properties are inferred and characterized (e.g., probabilistic distribution, spatial structure). At a CPT sounding, the empirical liquefaction model described in Section 3 will be used to evaluate the damage potential of liquefaction, quantified here by the liquefaction potential index (LPI). The two approaches described in Section 1, i.e., *the averaged index approach* and *the local soil property approach*, are developed to incorporate soil variability into the evaluation of liquefaction over an extended area. Details of multiscale random field model development and implementation will be discussed in Section 4. Finally, Monte Carlo simulations will be used to generate realizations of the random fields and results will be used for the probabilistic and spatial assessment of various quantities of interest for liquefaction evaluation over the region.

3. CPT-based liquefaction evaluation

In this work, we adopt the classical procedure proposed by Robertson and Wride [27] and subsequently updated by Robertson [28] and Ku et al. [29] to evaluate the liquefaction resistance of sandy soils based on CPT data. Herein, the liquefaction potential of a soil layer is evaluated using two variables - the cyclic stress ratio (CSR) and the cyclic resistance ratio (CRR). Details of CSR and CRR calculation are summarized in Appendix A.

Once CSR and CRR are obtained, the factor of safety (FS) against liquefaction triggering at a particular depth z can be calculated

$$\mathrm{FS} = \frac{\mathrm{CRR}}{\mathrm{CSR}} \tag{1}$$

which is then used in the subsequent liquefaction potential evaluation.

In this work, the potential of liquefaction damage will be quantified by an averaged index property, i.e., the liquefaction potential index (LPI), which was originally proposed by Iwasaki et al. [4,30] and has been subsequently used and calibrated by many investigators, e.g. [31–34,20,21,13,24,17]. As pointed out by Juang et al. [34] and more recently by van Ballegooy et al. [35,24], cautions should be taken when interpreting LPI results based on Iwasaki's criteria [4,30], which is based on liquefaction evaluation procedures commonly used in Japan in 1978. Nevertheless, in the current framework, the LPI is used as an averaged index to quantify potential liquefaction damage, the implications of using different liquefaction criteria and calibration of LPI models are discussed in more details in [34,35,24]. The detailed steps to calculate LPI are listed in Appendix B.

LPI can be used to classify the severity of liquefaction according to categories proposed by Sonmez [31] as shown in Table 1.

4. Multiscale random field characterization

The CPT-based empirical liquefaction model described in Section 3 evaluates the liquefaction potential at individual locations at the small scale, e.g., the borehole scale. To estimate the extent of liquefaction risk over the entire region of interest, multiscale random field models are introduced and implemented in this section.

4.1. Spatial correlation

In this study, the spatial correlation of geotechnical parameters is described using the semivariogram, $\gamma(\boldsymbol{h})$, which is equal to half the variance of the difference of two random variables separated by a vector distance $\boldsymbol{h}$

$$\gamma(\boldsymbol{h}) = \frac{1}{2}\mathrm{Var}[Z(\boldsymbol{u}) - Z(\boldsymbol{u}+\boldsymbol{h})] \tag{2}$$

where $Z(\boldsymbol{u})$ is a Gaussian random variable at location $\boldsymbol{u}$. The vector $\boldsymbol{h}$ accounts for both separation distance and orientation and therefore can be used to simulate anisotropic random fields. Here, we define a simplified scalar measure h

$$h = \sqrt{\left(\frac{h_x}{a_x}\right)^2 + \left(\frac{h_y}{a_y}\right)^2 + \left(\frac{h_z}{a_z}\right)^2} \tag{3}$$

where h_x, h_y and h_z are the scalar component of the vector $\boldsymbol{h}$ along the field's principal axes; scalar quantities a_x, a_y and a_z specify how quickly spatial dependence decreases along those axes.

In previous studies of liquefaction evaluation, e.g., [12,13,16], the correlation $\rho(h)$ is used to describe the spatial dependence of two parameters separated by h and can be related to the semivariogram as

$$\rho(h) = 1 - \gamma(h) \tag{4}$$

In practice, various analytical semivariogram models and their linear combinations are typically fitted to empirical semivariogram that is calculated from field data. Examples of commonly used analytical semivariogram models include the nugget effect model, the linear model, the spherical model, the exponential model and the Gaussian model [6]. Specific model form can be inferred from available field data

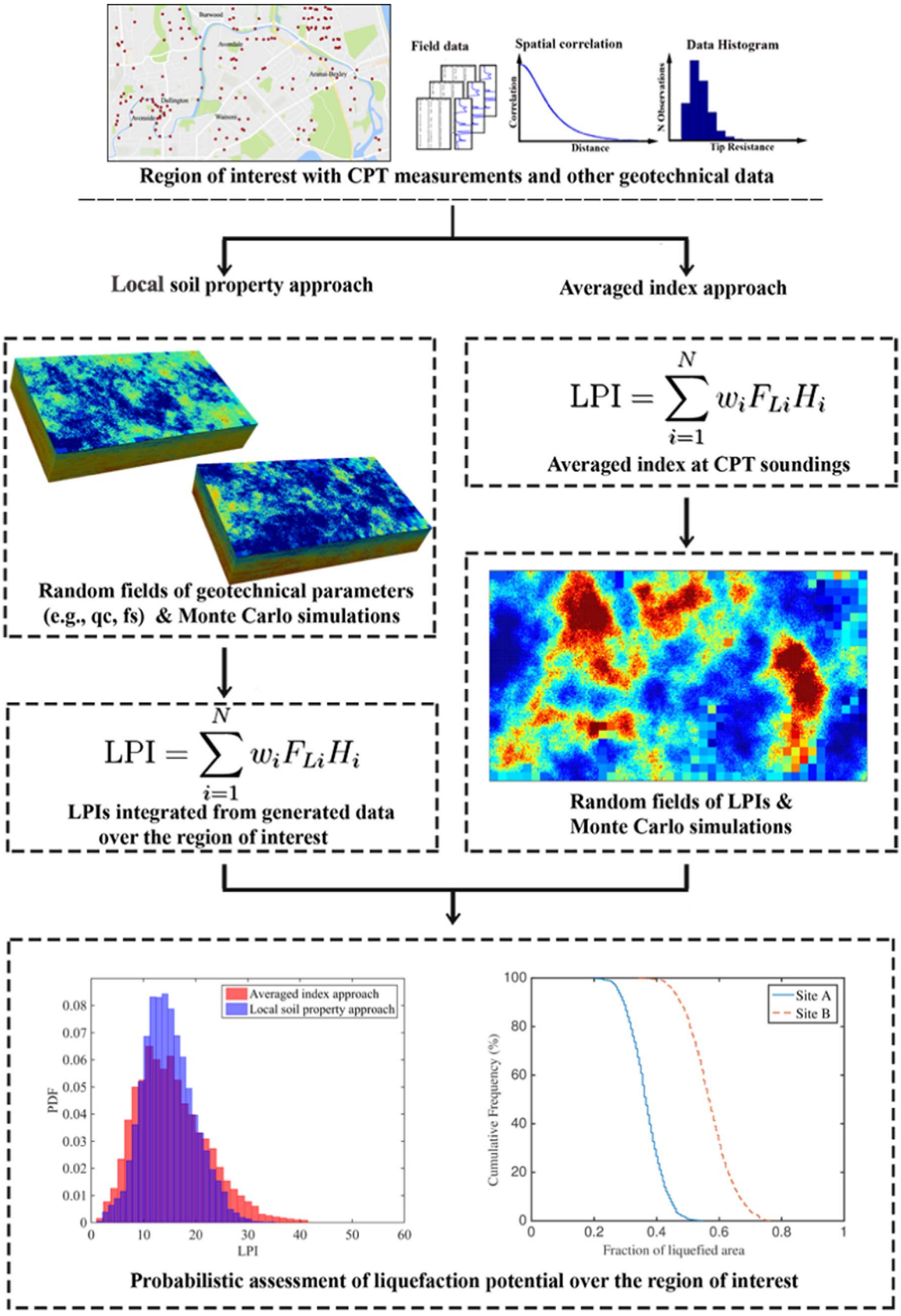

Fig. 1. General framework of the CPT-based liquefaction potential evaluation over extended area: the local soil property approach vs. the averaged index approach.

or assumed based on expert knowledge of properties of interest. As an example, an exponential model is adopted in this work

$$\gamma(h) = 1 - \exp\left(-\frac{h}{a}\right) \tag{5}$$

Table 1
Liquefaction potential index classification.

LPI	Liquefaction severity class
LPI = 0	I: Non-liquefiable
0 < LPI ≤ 2	II: Low
2 < LPI ≤ 5	III: Moderate
5 < LPI ≤ 15	IV: High
LPI > 15	V: Very high

where a is the range parameter and $3a$ is the practical range, i.e., the distance at which the exponential semivariogram levels off [6].

Usually there is a nugget effect in the empirical semivariogram model due to measurement errors or sparse data. For example, an exponential model combined with a nugget effect is expressed as

$$\gamma(h) = \omega\left[1 - \exp\left(-\frac{h}{a}\right)\right] + \tau \tag{6}$$

where τ is the nugget, i.e., the variance at zero distance; $\omega + \tau$ is the sill, i.e., the constant semivariance beyond the range $3a$.

It should be noted that the spatial dependence introduced above is for variables having Gaussian distributions. For non-Gaussian distributions, inference of spatial structure is recommended to be performed on transformed data using a normal score mapping [6]. Such normal score mapping is a common practice in many applications of geostatistics and has previously been shown to preserve the prescribed spatial structure for lognormally distributed variables [25,26].

4.2. Sequential simulation process

Given a specified probability density function and spatial correlation model, a sequential simulation process [6,36] is adopted in this work to generate realizations of the random field across the region. Each value is simulated individually conditional upon known information as well as any previously simulated data points.

Denote $\mathbf{Z}_p$ as a vector of all known and previously simulated points in the random field and Z_n as the next point to be simulated, the sequential simulation process can be illustrated by

$$\begin{bmatrix} Z_n \\ \mathbf{Z}_p \end{bmatrix} \sim N\left(\boldsymbol{\mu}, \begin{bmatrix} \sigma_n^2 & \boldsymbol{\Sigma}_{np} \\ \boldsymbol{\Sigma}_{pn} & \boldsymbol{\Sigma}_{pp} \end{bmatrix}\right) \tag{7}$$

where $\sim N(\boldsymbol{\mu}, \boldsymbol{\Sigma})$ denotes the vector of random variables following a joint normal distribution with mean vector $\boldsymbol{\mu}$ and covariance matrix $\boldsymbol{\Sigma}$; σ_n^2 is the prior variance of the next simulated point; $\boldsymbol{\Sigma}_{np}$, $\boldsymbol{\Sigma}_{pn}$ and $\boldsymbol{\Sigma}_{pp}$ are the covariance matrices, where the subscripts 'n' and 'p' represent 'next' (as in next point to be simulated) and 'previous' (as in all previously simulated points), respectively. The covariance matrices are obtained by

$$\mathrm{COV}[Z_i, Z_j] = \rho_{ij} \cdot \sigma_i \cdot \sigma_j \tag{8}$$

where ρ_{ij} is the correlation between random variables Z_i and Z_j with standard deviations of σ_i and σ_j, respectively.

Using the above model for joint distribution, the distribution of Z_n conditional upon all previously simulated data is given by a univariate normal distribution with updated mean and variance

$$(Z_n | \mathbf{Z}_p = z) \sim N(\boldsymbol{\Sigma}_{np} \cdot \boldsymbol{\Sigma}_{pp}^{-1} \cdot z,\ \sigma_n^2 - \boldsymbol{\Sigma}_{np} \cdot \boldsymbol{\Sigma}_{pp}^{-1} \cdot \boldsymbol{\Sigma}_{pn}) \tag{9}$$

It is noted that $\boldsymbol{\Sigma}_{np} \cdot \boldsymbol{\Sigma}_{pp}^{-1}$ are essentially the weights assigned in the simple Kriging process [6]. For the realization, one value of Z_n is drawn at random from the posterior univariate normal distribution.

Once simulated, Z_n becomes a data point in the vector $\mathbf{Z}_p$ to be conditioned upon by all subsequent data locations. This process is repeated by following a random path to each unknown location until all the values in the field have been simulated. This sequential simulation process is beneficial for the proposed work because: (1) it preserves known information (e.g., field data) precisely at their locations in the simulated random field; and (2) it allows one to first simulate the field at only the coarse scale, then add simulation points at the fine scale probabilistically consistent with the previous coarse-scale realizations, a process we will detail in Sections 4.3 and 4.4.

4.3. Multiscale spatial correlation

The multiscale spatial correlation is based on the notion that material properties at the coarser scales are the arithmetically averaged values of the properties over corresponding areas at the finer scales. This relation allows for the explicit derivation of variances and spatial correlation of quantities of interest between different scales and is visually represented in Fig. 2.

For two scales of interest, we denote the coarser scale as scale 'c' and the finer scale as scale 'f'. The cross-scale spatial correlations can then be calculated as [17]

$$\rho_{Z_I^f, Z_{II}^c} = \frac{\sum_{i=1}^{N}\sum_{k=1}^{N} \rho_{Z_{i(I)}^f, Z_{k(II)}^f}}{\sqrt{\sum_{i=1}^{N}\sum_{j=1}^{N} \rho_{Z_{i(I)}^f, Z_{j(I)}^f}} \sqrt{\sum_{i=1}^{N}\sum_{j=1}^{N} \rho_{Z_{i(II)}^f, Z_{j(II)}^f}}} \tag{10}$$

$$\rho_{Z^f, Z_I^c} = \frac{\sum_{i=1}^{N} \rho_{Z^f, Z_{i(I)}^f}}{\sqrt{\sum_{i=1}^{N}\sum_{j=1}^{N} \rho_{Z_{i(I)}^f, Z_{j(I)}^f}}} \tag{11}$$

where $\rho_{Z_I^c, Z_{II}^c}$ = correlation between two coarse-scale elements I and II; ρ_{Z^f, Z_I^c} = correlation between a fine-scale element and a coarse-scale element I.

The geotechnical properties will be simulated using random field models at the coarse scale (e.g., the regional scale), and then adaptively refined into smaller scales (e.g., the borehole or structure scales), conditional upon the coarse-scale random field simulations. It is worth noting that the cross-scale correlations (10) and (11) are applicable to general non-uniform arbitrary shaped grids and actual field CPT-based geotechnical measurements will be incorporated into the sequential simulation process.

4.4. Numerical implementation

The previously described CPT-based empirical liquefaction model in Section 3 as well as the random field models in the current section are implemented in a computer code written in Matlab. Details of the

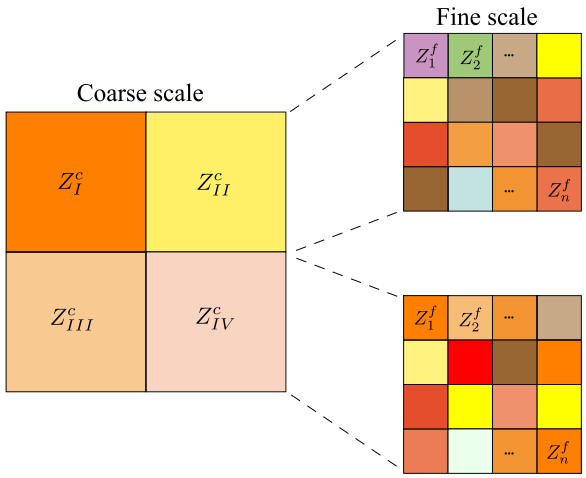

Fig. 2. Graphic representation of material properties at two scales. The superscripts 'c' and 'f' refer to 'coarse' and 'fine' scales, respectively. The subscripts refer to the element number. Roman letters *I*, *II*… are used for coarse scale element and Arabic numbers 1, 2, 3… are used for fine scale element.

numerical implementation and some common measures to improve the computational efficiency of random field generation are discussed in this section.

The flowchart of the multiscale random field implementation is shown in Fig. 3. The program requires as inputs: the random field parameters (e.g., the probability model, the semivariogram model), the geometry of the region and an initial grid, and any available field data for the conditional simulation of unknown data. Defining an initial grid allows convenient refinement of an initial coarse random field into higher resolution fine scale fields following the procedure described in Section 4.3. The random variable is simulated at the centroid of each cell and its value is assigned to the corresponding cell. The end product or output of the program is a multiscale random field realization for quantities of interest within the region of interest.

The conditional sequential simulation process adopted in this work preserves the known field data at their locations and allows all subsequent generated data points to be conditioned upon such known information and any previously generated points. One drawback with this process, however, is that it can be quite computationally demanding. Several common measures are implemented in this work to improve the computational efficiency of the simulation.

First, the fine scale random fields are only selectively generated at locations that are deemed necessary for higher resolution information. Examples of such locations include areas around CPT soundings or near important buildings. The sequential simulation process described above has the benefit of selective and adaptive refinement. If deemed necessary at any point in simulation process, any coarse scale element at any location can be refined into its fine-scale components without consideration of the refinement sequence.

Second, the size of the matrix containing previously simulated data $\boldsymbol{Z}_p$ in Eqs. (7) and (9) will be limited by taking advantage of the screening effect. The screening refers to the phenomenon of dramatically reducing the Kriging weight assigned to a datum that is screened by another nearby data near the location being simulated [37]. After the nearest data, other more distant data will receive little weight even if they are correlated with the location under consideration.

Fig. 4(a) plots the weights assigned to the neighbours of the data point $\boldsymbol{Z_n}$ to be simulated with and without limiting the size of the matrix $\boldsymbol{Z}_p$ containing previously simulated points. “Screened to 30” means the nearest 30 data points are included in the covariance matrix calculation. In this work, including the nearest 30 data points is sufficient since more distanced points have been assigned negligible weights. This is consistent with previous experience and recommendation in [37]. Also, it is important to note that limiting the size of the matrix $\boldsymbol{Z}_p$ does not adversely affect the spatial correlation, as shown in Fig. 4(b). The slight difference between the specified and empirical semivariogram is partially due to the relatively small field size.

As a third method to further improve computational efficiency, it is noted that the covariance matrices in Eq. (9) only depend on the relative locations between pairs of data points in the random field. Therefore, if the locations of coarse and fine scale data points are known and fixed between different simulations, those covariance matrices need to be computed only once and can be reused by all subsequent simulations. This will significantly reduce computation time when the random field simulation is used within a Monte Carlo framework, where thousands of simulations are typically per-

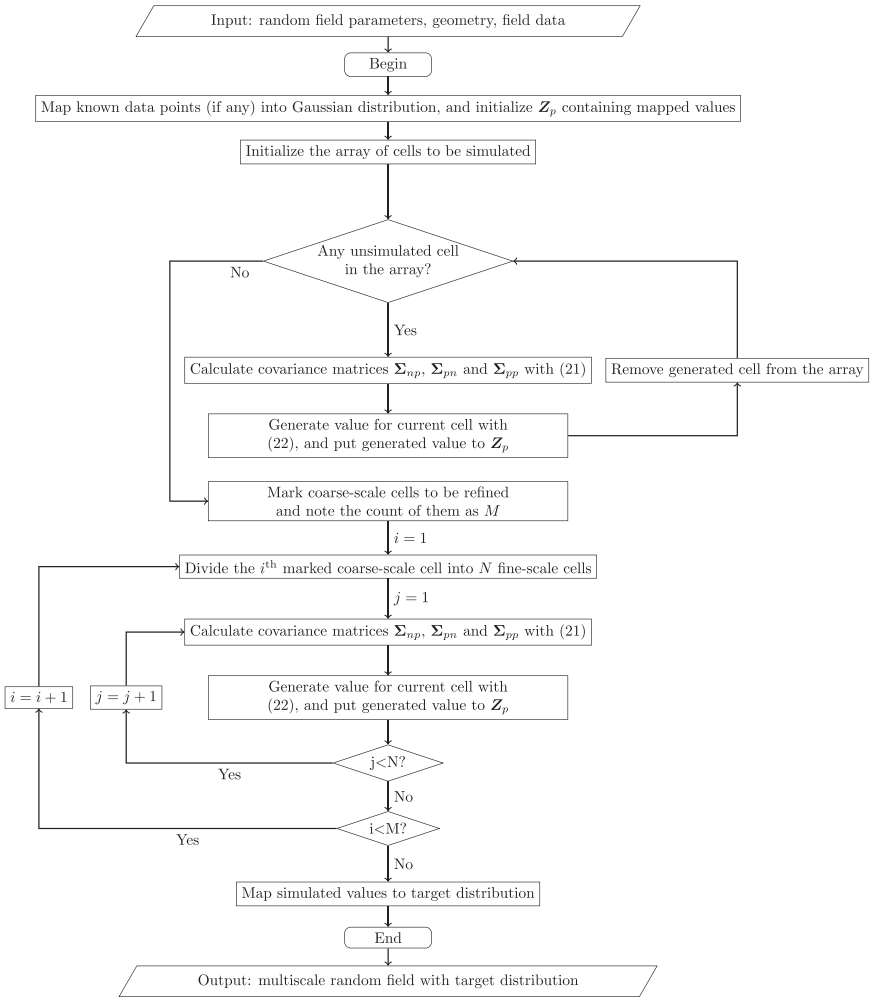

Fig. 3. Flowchart of the multiscale random field model implementation.

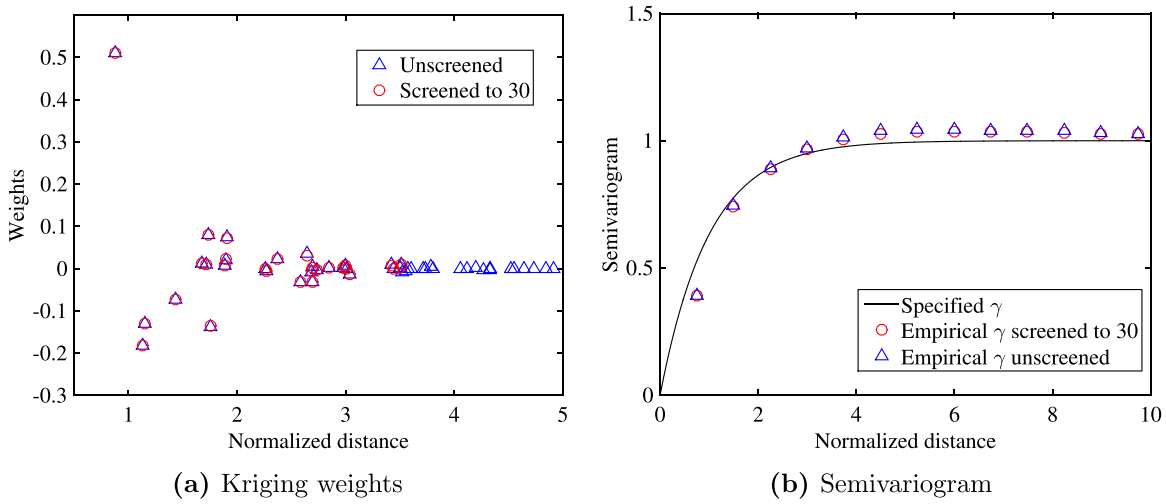

(a) Kriging weights (b) Semivariogram

Fig. 4. Screening effect on the data point Z_n to be simulated: (a) Kriging weights assigned to neighbours of Z_n with and without limiting the size of the matrix containing previously simulated points; (b) specified and empirical semivariogram calculated from one realization of random field. The distance is normalized by the correlation length parameter '*a*'.

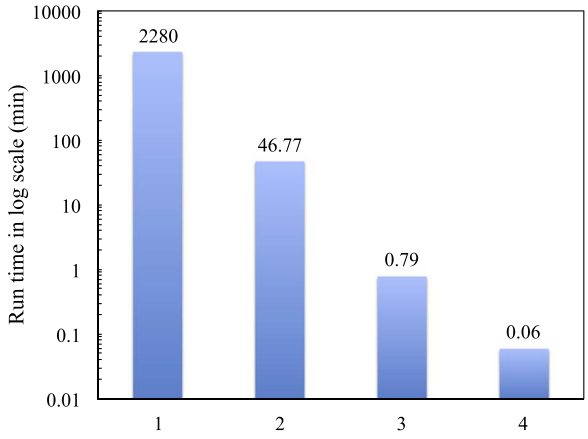

Fig. 5. Computational efficiency comparison. Case 1: all coarse elements are included for refinement, without any optimization; case 2: selective refinement, without any optimization; case 3: selective refinement, with screening to the nearest 30 elements; case 4: selective refinement, pre-calculated covariance matrices and with screening.

formed.

Fig. 5 shows the comparison of computation time in log scale before and after measures are taken to improve computational efficiency. The computation is performed on one computing node of Clemson University's Palmetto Cluster, with 1 CPU (Intel(R) Xeon(R) L5420@ 2.50 GHz) and 24 Gb RAM. Orders of magnitude improvement in computational efficiency are achieved. Further improvement can be realized by taking advantage of recent parallel computing capabilities added to Matlab, which will be left for future studies.

5. Numerical examples

In this section, the developed multiscale random field model is applied to evaluate liquefaction potential in the city of Christchurch, New Zealand. The purpose of the numerical examples is twofold: (1) to demonstrate the applicability of multiscale random field models in liquefaction evaluation over extended areas; (2) to assess *the averaged index approach* and *the local soil property approach* in accounting for the spatial variability of CPT-based geotechnical parameters and their implications on the liquefaction evaluation. We assume the stationary of the random field model and focus mainly on the spatial variability of tip resistance, side friction and the liquefaction potential index. Spatial variability of other geotechnical parameters, e.g., water table and unit weight of soil, are not included in the current study.

5.1. Analysis region and field data

Christchurch, New Zealand, is a city founded on the boundary of the alluvial Springston formation and the marine Christchurch formation [38]. During the period between September 2010 and December 2011, the city of Christchurch was strongly shaken by a sequence of four

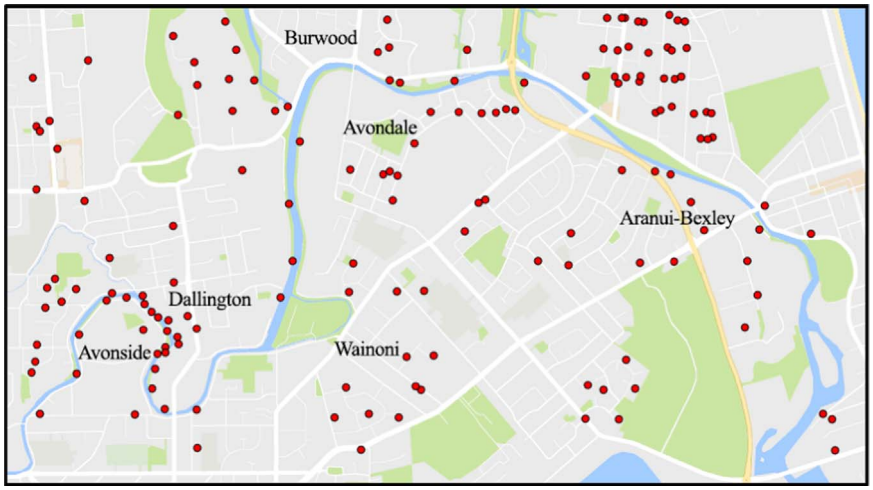

Fig. 6. Map of the area of study in Cristchurch, New Zealand. Red dots represent locations of the 155 CPT soundings.

strong earthquake events known as the Canterbury earthquakes. For the following liquefaction analysis and liquefaction potential mapping, we pick one of the great events, the February 17, 2011 earthquake event. The moment magnitude of the earthquake M_w=6.2. Typical peak ground surface acceleration a_{max} in the the area of study ranging from 0.34g to 0.50g [39]. A median value of a_{max} = 0.42 g is used in the following liquefaction potential calculations. A total of 155 CPT profiles with measured water table are collected from the New Zealand Geotechnical Database (NZGD). The locations of the CPT soundings are shown in Fig. 6. An averaged moist unit weight of γ_m = 18.5 kN/m^3 is used for soils above water table and an saturated unit weight of γ_{sat} = 19.5 kN/m^3 is used for soils below water table following information presented in [40].

5.2. Random field realizations – the averaged index approach

The first set of random field realizations is generated following the *the averaged index approach*. Herein, the liquefaction potential index (LPI) will be calculated at every CPT sounding location using the CPT-based empirical liquefaction model described in Section 3.

Fig. 7 shows the histogram and semivariogram of the calculated LPIs at 155 CPT sounding locations. As can be seen from Fig. 7(a), most of the LPI at the 155 CPT soundings are greater than 5, indicating that majority of those CPT sounding sites have a high liquefaction severity class (refer to Table 1). The spatial structure of the LPIs is fitted using the exponential model defined in Eq. (6) with the following fitted parameters: a=498.70 m, ω = 0.74, τ = 0.22. A weighted least square method by Cressie [41] is used to fit the exponential model parameters.

In the subsequent random field realizations, the LPI will be treated as the random variable of interest and its values throughout the Christchurch site will be generated using the sequential simulation process described in Section 4.2. The fitted exponential semivariogram model as shown in Fig. 7(b) will be used to describe the spatial correlation. Given the site specific model and model parameters, random field simulations are performed. Typical realizations of LPIs across the Christchurch site are shown in Fig. 8 for both single and multiscale random fields. The calculated LPI values at CPT soundings are preserved at those locations. It is shown, as expected, that the multiscale random field captures more local fluctuations of LPIs than the single scale in areas where higher levels of resolutions are taken into account. Such a fine scale resolution is important especially for site-specific liquefaction susceptibility and hazard evaluation as will be illustrated later.

The histogram and empirical semivariogram corresponding to the LPI random field realizations in Fig. 8(b) are shown in Fig. 9. The histogram has a lognormal distribution shape. The empirical semivariogram is calculated from the generated LPI random field, which preserves the specified exponential spatial structure.

5.3. Random field realizations – the local soil property approach

In the second set of random field realizations, CPT-based geotechnical parameters, i.e., the CPT tip resistance q_c and the side friction f_s, are treated as spatially correlated random variables. Their values will be realized using the sequential simulation process described in Section 4.2. Fig. 10 shows the empirical semivariograms of q_c and f_s. The spatial structures of those CPT parameters are fitted using the exponential model defined in Eq. (6) with the following model

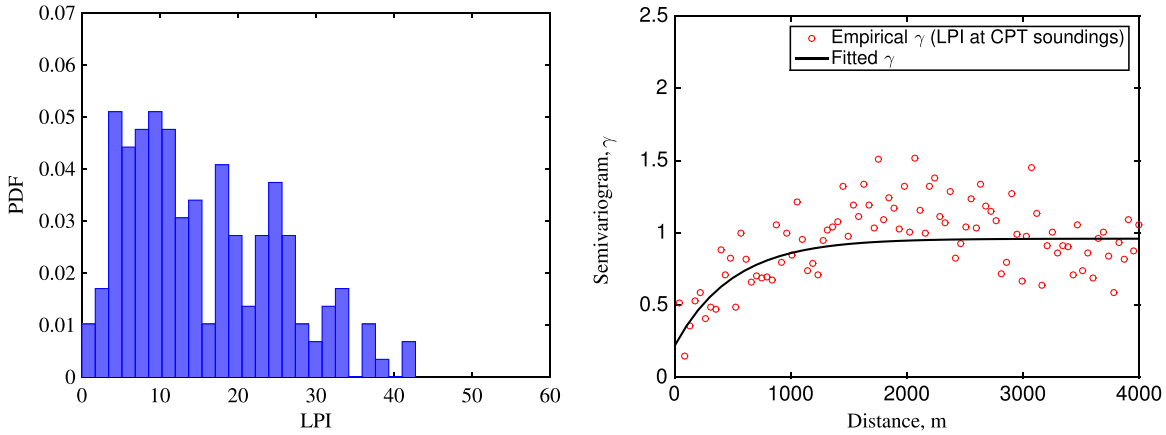

Fig. 7. Histogram and semivariogram of calculated LPIs at 155 CPT sounding locations.

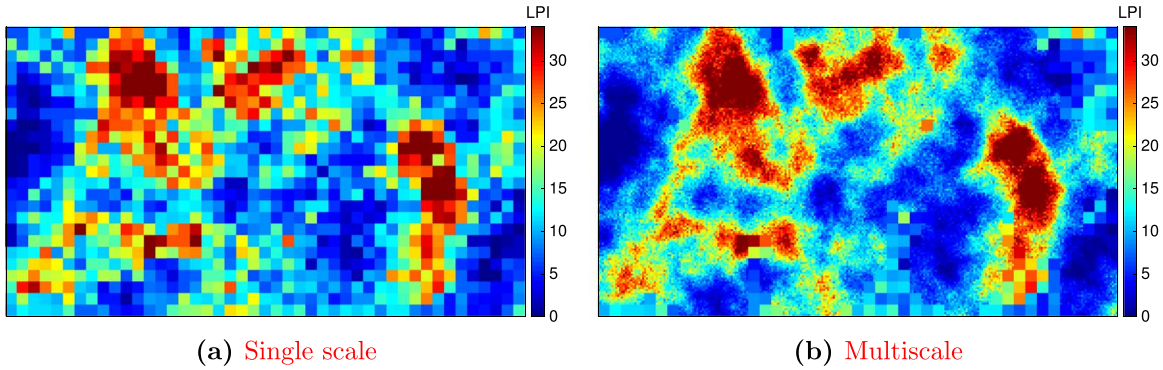

Fig. 8. Typical random field realizations of LPIs following the averaged index approach.

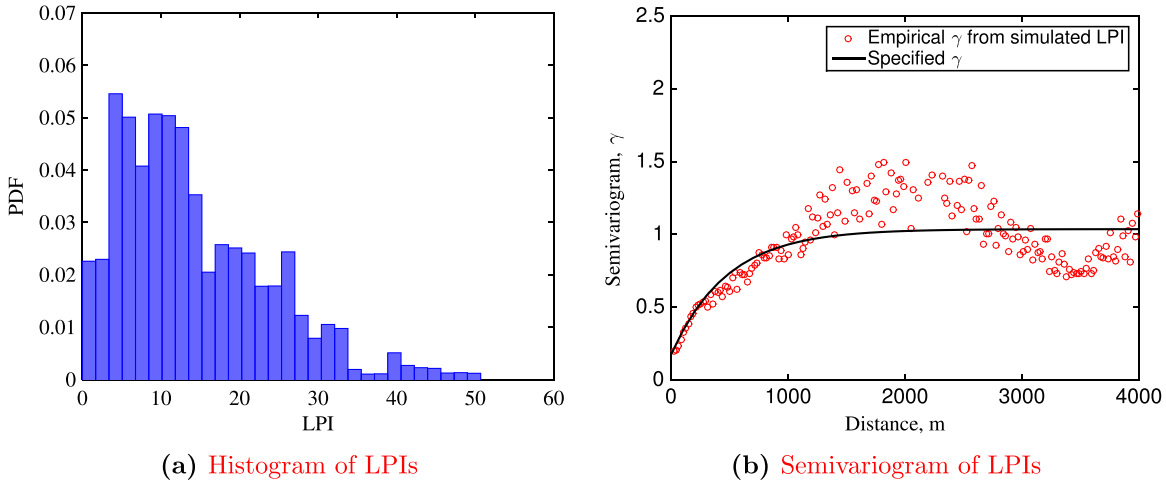

Fig. 9. Typical histogram and semivariogram of LPIs following the averaged index approach.

parameters: for the tip resistance q_c, a = 339.6 m, ω = 0.60, τ = 0.44; for the side friction f_s, a = 316.23 m, ω = 0.47, τ = 0.55. The probability distribution are inferred directly from the CPT data.

Random field simulations are performed for each soil layer with a thickness of 0.2 m. Fig. 11 shows typical multiscale random field realizations of q_c and f_s for one soil layer at 10 m below the ground surface. Typical multiscale realizations of q_c and f_s values across the Christchurch site for all soil layers within the first 20 m below the ground surface are shown in Fig. 12.

With the calculated q_c and f_s values at each location within the Christchurch site along with assumed constant unit weights, the LPIs can be calculated following the method stated in Section 3. One set of LPI field across the area of study is shown in Fig. 13. It can be seen that the multiscale random field captures the similar spatial distribution of LPIs across the region to that of the single scale random field. Moreover, there are higher resolutions of LPIs in selected area of interest. Such higher level resolution is important for local liquefaction analysis.

The histogram and semivariogram of the multiscale random field realization in Fig. 13(b) are shown in Fig. 14(a) and (b), respectively. It should be noted that, in the local soil property approach, the simulated LPIs are not expected to preserve the specified spatial correlation structure of q_c and f_s due to the nonlinear transformation in the empirical liquefaction model described in Section 3. In the averaged index approach, the simulated LPIs are expected to preserve the spatial structure inferred from calculated LPI values at 155 CPT sounding locations. This is verified by Fig. 14(b), which shows the empirical semivariogram calculated from simulated LPIs across the site and the specified exponential model.

5.4. Probabilistic and spatial assessment of liquefaction potentials

In the previous two sections, we have demonstrated typical random field realizations of LPIs by the averaged index approach and the local soil property approach. In this section, we will perform Monte Carlo simulations and assess the implications of two approaches on the probabilistic and spatial characteristics of liquefaction potentials in the Christchurch site. In addition, utilizing multiscale random field realizations, liquefaction evaluation will be performed for selected local sites to demonstrate the advantage and applicability of proposed methodology.

A total of 1000 Monte Carlo simulations are performed to generate realizations of LPIs across the Christchurch site. Fig. 15(a) shows the histogram of the averaged LPIs from 1000 Monte Carlo simulations and Fig. 16 shows the corresponding maps of the averaged LPIs. To attenuate the effect of ergodic fluctuations, empirical semivarograms are calculated 1000 times, averaged, and plotted in Fig. 15(b). The solid curve is the specified exponential model with parameters fitted using LPIs at CPT soundings. The red dots and blue squares are the empirical semivariograms calculated using Eq. (2) with LPI values generated by the averaged index approach and the local soil property approach, respectively. The error bars (± one standard deviation) show the variations of 1000 Monte Carlo simulations. Fluctuating semivariogram is resulted from weak and unsteady correlation of properties

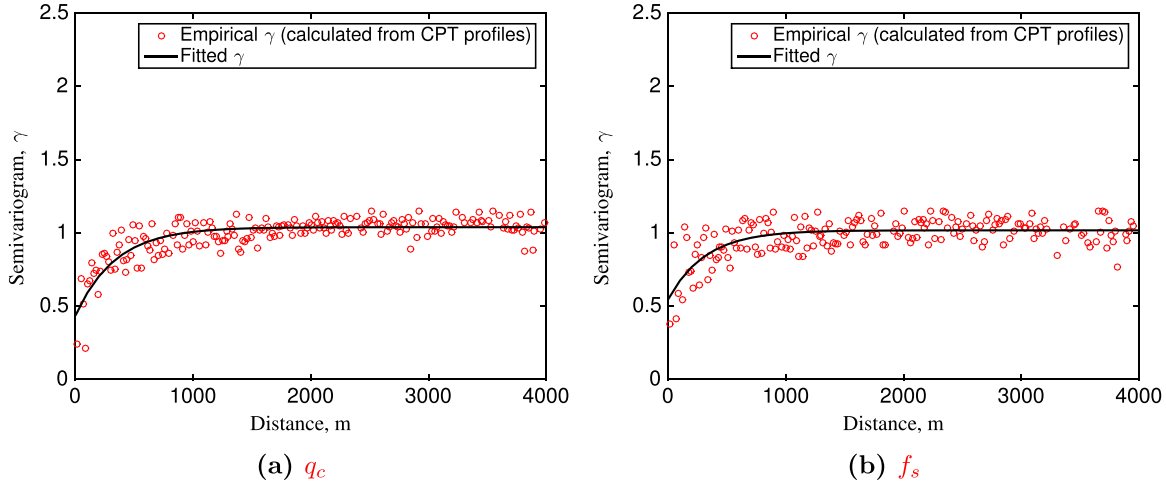

Fig. 10. Semivariograms of the tip resistance q_c and the side friction f_s calculated from 155 CPT soundings.

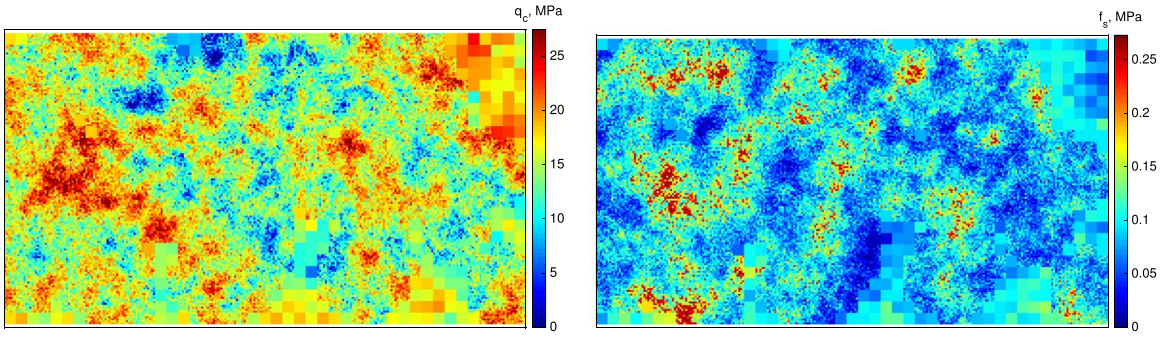

Fig. 11. Typical multiscale random field realizations of q_c and f_s in one soil layer (at the depth of 10 m).

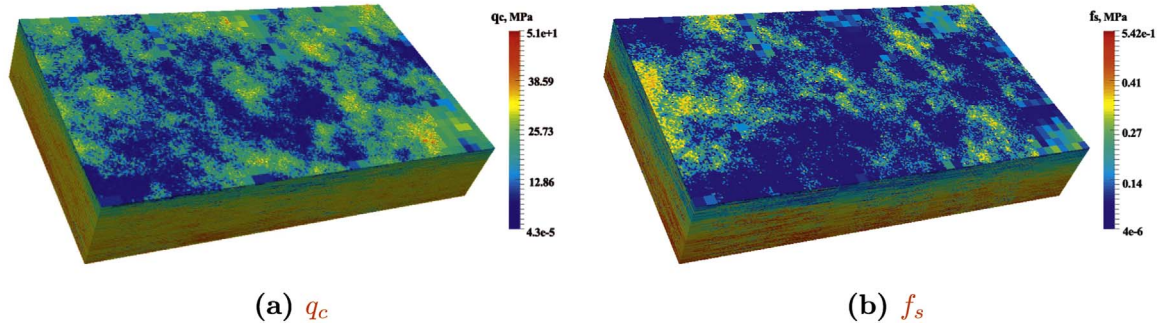

Fig. 12. Typical multiscale random fields of q_c and f_s in three dimensions.

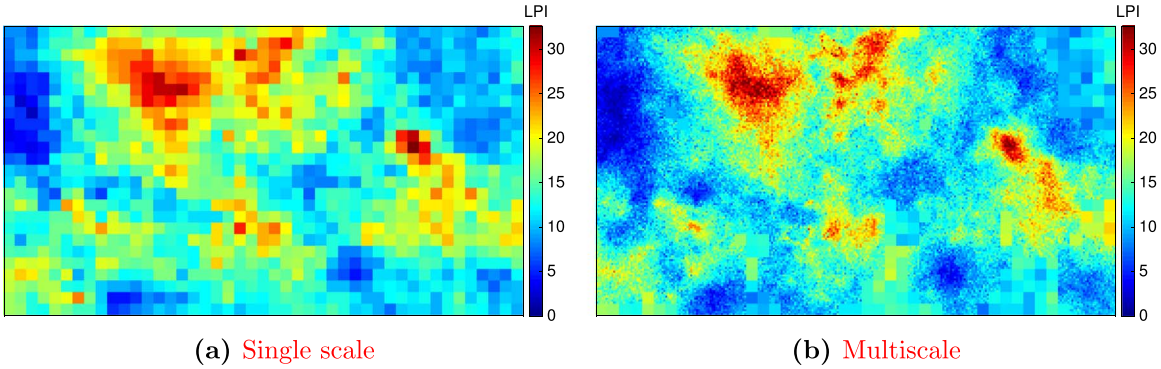

Fig. 13. Typical random field realizations of LPIs following the local soil property approach.

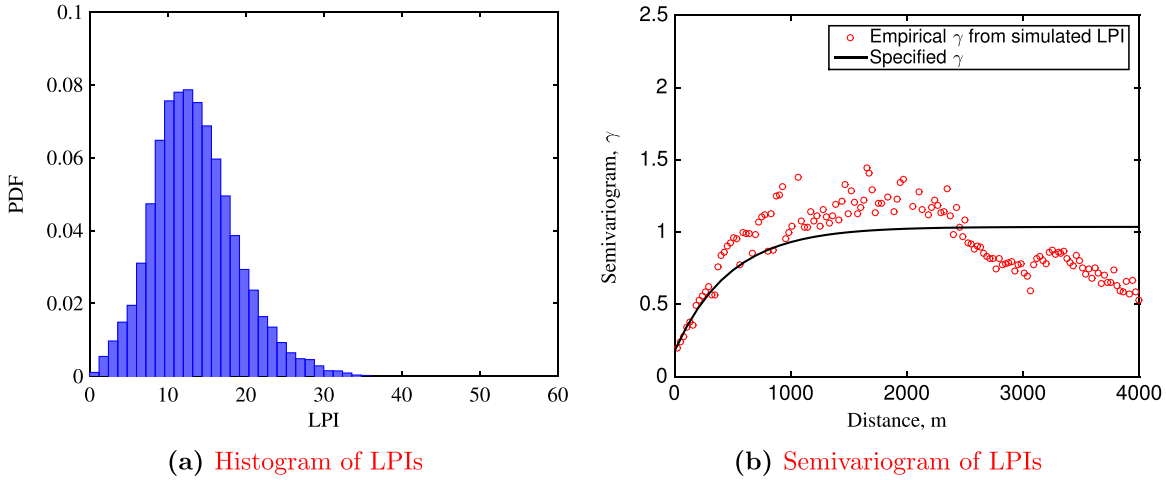

Fig. 14. Typical histogram and semivariogram of LPIs following the local soil property approach.

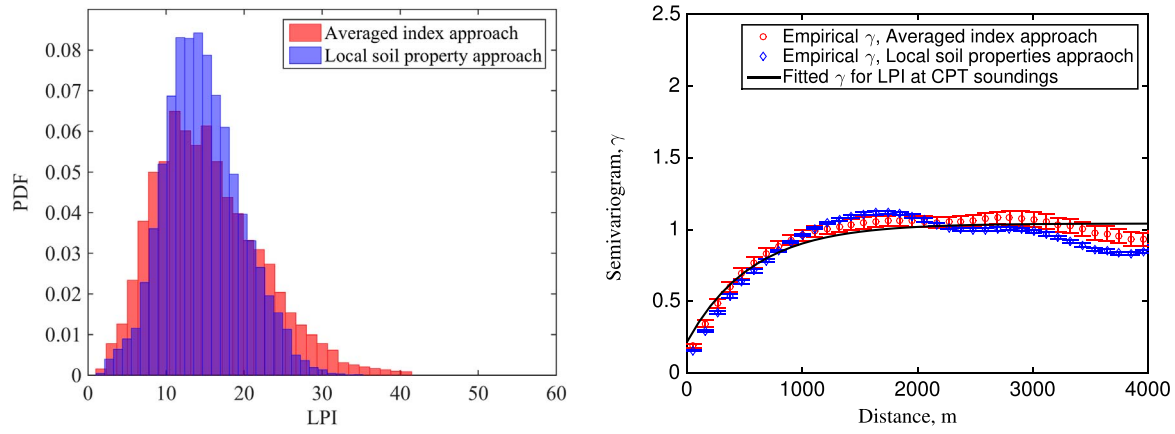

(a) Histograms of LPIs (b) Semivariograms of LPIs

Fig. 15. Histograms and semivariograms of the averaged LPIs from 1000 Monte Carlo simulations. Error bars in semivariogram plot indicate ± one standard deviation.

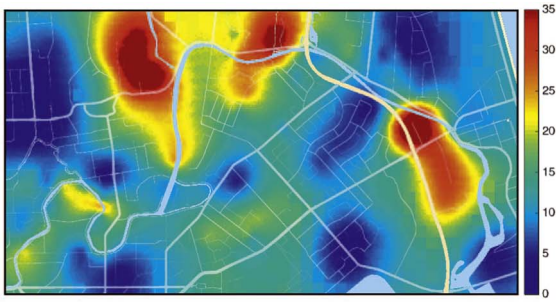

(a) Averaged index approach

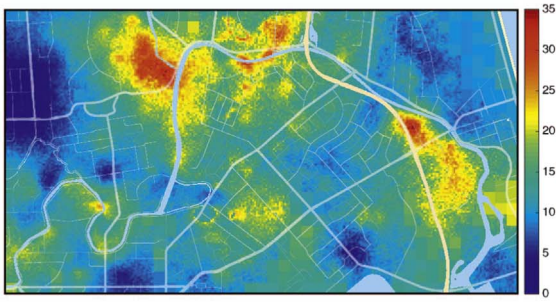

(b) Local soil property approach

(c) Observations: i. No observed ground cracking or ejected liquefied material; ii. Minor ground cracking but no observed ejected liquefied material; iii. No lateral spreading but minor to moderate quantaties of ejected material; iv. No lateral spreading but large quantities of ejected material; v. Moderate to major lateral spreading; ejected material often observed; vi. Severe lateral spreading; ejected material often observed. [42]

Fig. 16. Mapping of LPI by two approaches compared with the observed liquefaction phenomenons.

between separated places. This is verified in Fig. 15(b), i.e., great fluctuations (in both the average and standard deviation) of the empirical semivaiograms are observed at distance greater than 1000 m. The local soil property approach results in slightly greater fluctuation of semivariogram possibly due to the nonlinear transformation from q_c and f_s to LPI.

The generated LPI maps by two different approaches are compared with the map of observed liquefaction phenomenons after the February 17, 2011 earthquake event [42], as shown in Fig. 16. Comparing the maps of predicted LPIs against the observations, it can be seen that both the averaged index approach and the local soil property approach are able to capture the varying severity levels of liquefaction at most locations across the area of study. For instance, the high LPI value area corresponds well with areas with observed moderate to several liquefaction. The results by the local soil property approach shows more small scale fluctuations or "noises". This is due to the high nugget effects in the specified semivariograms of q_c and f_s.

Results from Monte Carlo simulations can also be used for the probabilistic assessment of liquefaction potentials. Various quantities of interest can be defined. As an example, we evaluate the cumulative frequency distributions of LPIs following the methodology proposed in [20].

Fig. 17 plots the cumulative frequencies of LPIs in the area of study obtained with the averaged LPI map from 1000 Monte Carlo simulations. The error bars (± one standard deviation) are also included in the cumulative frequency plots. It can be seen that the cumulative frequency curve by the averaged index approach is very close to that of the known LPI obtained from 155 CPT soundings, while a sharp change in the slope of the cumulative frequency curve for the local soil property approach is observed, which can be explained by its histogram in Fig. 15(a). Most of the LPIs simulated by this approach fall between 10 and 20, resulting in a sharp change in cumulative frequency curve in this range. For the averaged index approach, the percentages of different LPI values are more "spread-out", which results in smoother cumulative frequency curves.

Comparisons between Fig. 17(a) and (b) indicate that multiscale random fields yield consistent results as the single scale counterparts for cumulative frequencies of LPIs. This is to be expected given the notion that properties of a coarse element are the averaged values of the properties over the corresponding areas at the fine scale.

It should be noted that all previous analysis and comparisons are based on relatively sufficient field data to infer random field model parameters. It is expected that the amount of the field will impact the results of the random field-based liquefaction mapping. While this subject itself deserves a future study, for this Christchurch site, we investigated the effect to data availability on the distribution of

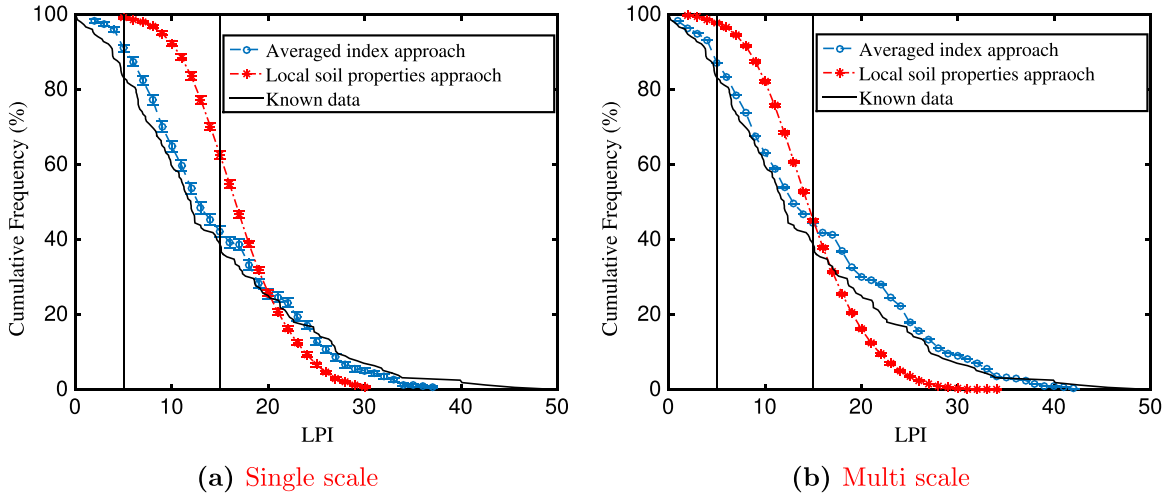

Fig. 17. Cumulative frequency plot of LPIs for the area of study in Christchurch.

predicted LPIs in the area of study. The number of available CPT soundings are varied from 9 to 243. It is found that when the number of CPT soundings is small, the local soil property approach yields higher mean LPI values. As the number of CPT soundings increase, the distributions obtained from the averaged index approach and the local soil approach converge. Fig. 18 plots the histogram of LPIs obtained with 9 CPT and 69 CPT soundings.

5.5. Fine-scale site-specific liquefaction assessment

The final analysis involves the fine-scale site-specific liquefaction assessment. Compared to single scale random field, multiscale random field provides higher resolution at local or site-specific scale, e.g., near a critical infrastructure or a particular building of interest. To illustrate this point, we evaluate the liquefaction potential at two local sites in Christchurch. The site locations are shown in Fig. 19. Site A is a small region consists of two schools, i.e., the Chisnallwood Intermediate School and the Avondale Primary School. Site B is the location of the Aranui High School. The inset of random fields in Fig. 19 shows that the multiscale random field could provide much more detailed information than the single scale counterpart, which makes it possible to perform site-specific liquefaction evaluation while consistently maintaining predictions of liquefaction for the entire region over much larger scales.

Based on the cumulative frequency distribution, Holzer et al. [20] proposed that for a given geologic unit, the percent area predicted to have liquefaction during a given earthquake-shaking scenario could be estimated from the cumulative frequency distributions at LPI ≥ 5. This criteria can be further categorized to indicate percentage of area to have minor liquefaction (5 ≤ LPI < 15) and major liquefaction (LPI ≥ 15) as shown in Table 1. Herein, the percentage of areas in the selected sites with LPI ≥ 15 under a given earthquake-shaking scenario (M_w=6.2, a_{max} = 0.42 g) is calculated and plotted against the corresponding cumulative frequency in Fig. 20.

Fig. 20 shows cumulative frequencies of LPIs with respect to the fraction of liquefied area. The cumulative frequency curve for site B is consistently 'higher' than site A for both the averaged index approach and the local soil property approach, indicating that site B is more likely to liquefy than site A in a given earthquake. Comparisons between two approaches show that the cumulative frequency for the average index approach is more "spread-out" than the local soil property approach. This is consistent with the the predictions within the whole site of Christchurch, as shown in Fig. 17.

The above analysis on the percentage of the liquefiable area underneath a particular site gives an indication of the implied reliability of the site with respect to liquefaction resistance during a given earthquake. These site-specific curves can only be obtained if a higher resolution multiscale random field is generated. Moreover,

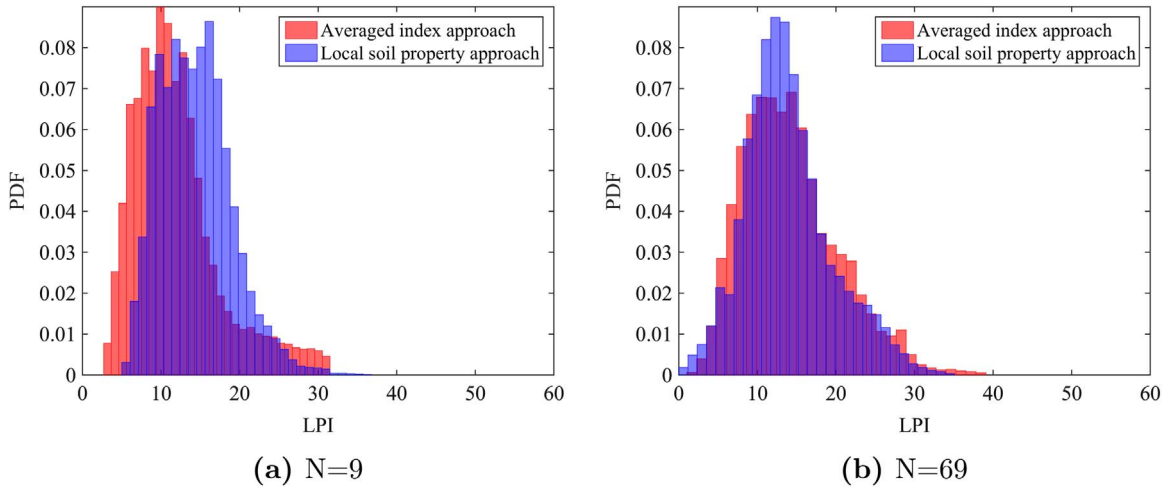

Fig. 18. Histograms of predicted LPIs in the Christchurch site when different number of CPT soundings (N) is used to infer model parameters.

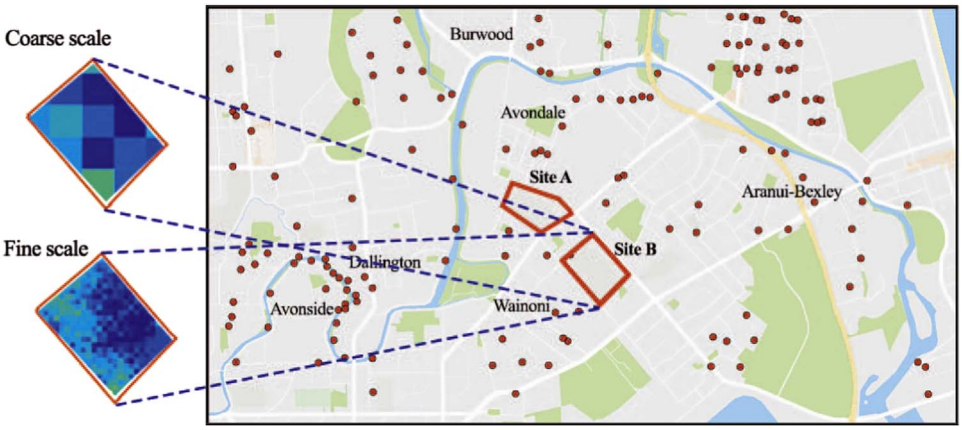

Fig. 19. Locations of two selected sites for fine-scale liquefaction assessment.

multiscale random fields is able to obtain high-resolution information at local site while consistently maintaining low-resolution information at much larger scales, leading to a computationally efficient process.

Finally, it should be noted that the methodologies discussed in this study is sufficiently general to be applied to other earthquake-prone areas and to evaluate quantities of interest such as liquefaction-induced settlement, lateral spreads or site conditions [44]. This is being explored in further studies.

6. Conclusions

In this paper, a classical CPT-based empirical liquefaction model and multiscale random field models are integrated for the assessment of regional liquefaction susceptibility. The study focuses on the spatial variability of CPT-based geotechnical parameters. Two approaches, termed *the averaged index* approach and *the local soil property* approach, are developed and analyzed to account for spatial variability of geotechnical parameters. Their implications on liquefaction susceptibility evaluation are discussed through one case study at the Christchurch site in New Zealand. In summary, it is found that

1. Both the averaged index and the local soil property approaches are able to capture the spatial variations of liquefaction potential at different scales over the area of study and predict qualitatively consistent results compared to previously reported liquefaction manifestations.
2. The two approaches yield similar and comparable LPI values for the area of study when sufficient CPT data is available. However, when the CPT data is sparse, the averaged index approach, in general, predicts lower LPI values when compared with the local soil property approach.
3. The averaged index approach is recommended for regional liquefaction evaluation given that it yields consistent results with field observations and is much more computationally efficient.
4. The local soil property approach, though providing more details on soil properties, requires much more field data to characterize random field models, which could introduce additional uncertainties into the solution.
5. Both approaches have been cast within a multiscale random field model, which allows efficient and effective assessment of site-specific liquefaction susceptibility.

Acknowledgment

The corresponding author wishes to acknowledge the financial support provided by the Shrikhande Family Foundation through the Shrikande Graduate Fellowship awarded to the first author. Clemson University is acknowledged for the generous allotment of computer time on Palmetto cluster.

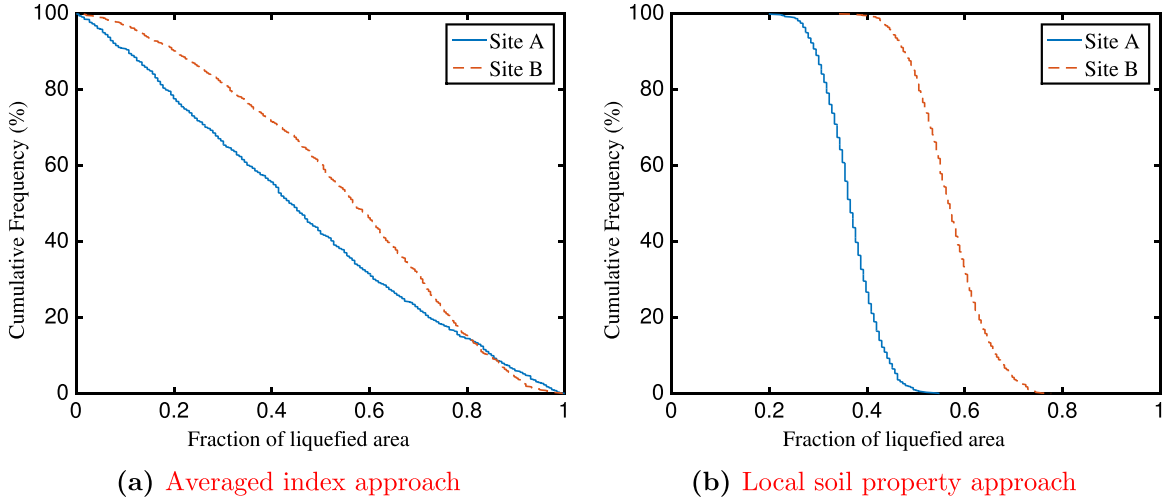

Fig. 20. Cumulative frequency vs. fraction of liquefied area with LPI ≥ 15 for two local sites A & B selected in the area of study.

Appendix A. The updated Robertson and Wride 1998 liquefaction model

For CSR, the following adjusted form is recommended in [3]

$$\mathrm{CSR} = 0.65\left(\frac{a_{\max}}{g}\right)\left(\frac{\sigma_{\mathrm{vo}}}{\sigma'_{\mathrm{vo}}}\right)(r_d)\left(\frac{1}{\mathrm{MSF}}\right)\left(\frac{1}{K_\sigma}\right) \tag{A.1}$$

where $a_{\max}$ is the peak horizontal acceleration at the ground surface generated by a given earthquake; g is the gravitational acceleration; σ_{vo} and σ'_{vo} are the total and effective vertical overburden stresses, respectively; and r_d is the depth-dependent shear stress reduction coefficient; MSF is the magnitude scaling factor; K_σ is the overburden correction factor for the cyclic stress ratio ($K_\sigma = 1$ for $\sigma'_{\mathrm{vo}} < 1$ atm (1 atm=100 kPa)). CSR defined above is also often denoted as $\mathrm{CSR}_{7.5}$ for earthquakes with magnitudes of approximately 7.5. The stress reduction factor r_d and the magnitude scaling factor MSF are both estimated based on the recommendations in [3] as

$$r_d = \frac{1.000 - 0.4113z^{0.5} + 0.04052z + 0.001753z^{1.5}}{1.000 - 0.4177z^{0.5} + 0.05729z - 0.006205z^{1.5} + 0.001210z^2} \tag{A.2}$$

$$\mathrm{MSF} = \frac{10^{2.24}}{M_w^{2.56}} \tag{A.3}$$

where z is the depth; M_w is the moment magnitude of the earthquake.

The cyclic resistance ratio, CRR, is estimated from CPT data following the procedure in [27–29] as

$$\mathrm{CRR} = \begin{cases} 0.8333[(q_{c1N})_{\mathrm{cs}}/1000] + 0.05 & \text{if} \quad (q_{c1N})_{\mathrm{cs}} < 50 \\ 93[(q_{c1N})_{\mathrm{cs}}/1000]^3 + 0.08 & \text{if} \quad 50 \le (q_{c1N})_{\mathrm{cs}} < 160 \end{cases} \tag{A.4}$$

The equivalent clean sand normalized penetration resistance, $(q_{c1N})_{\mathrm{cs}}$ is given as

$$(q_{c1N})_{\mathrm{cs}} = K_c(q_{c1N}) \tag{A.5}$$

where the conversion factor K_c is calculated from the soil behavior type index I_c as

$$K_c = \begin{cases} 1 & \text{for} \quad I_c \le 1.64 \\ -0.403I_c^4 + 5.581I_c^3 - 21.63I_c^2 + 33.75I_c - 17.88 & \text{for} \quad I_c > 1.64 \end{cases} \tag{A.6}$$

and q_{c1N} is the normalized cone penetration resistance

$$q_{c1N} = \left(\frac{q_c - \sigma_{vo}}{P_{at}}\right)\left(\frac{P_{at}}{\sigma'_{vo}}\right)^n \tag{A.7}$$

where $P_{at} = 1$ atm of pressure (100 kPa); q_c is the measured cone penetration resistance; σ_{vo} and σ'_{vo} are the total and effective vertical overburden stresses, respectively. The stress exponent n is estimated as [28]

$$n = 0.381(I_c) + 0.05\left(\frac{\sigma'_{\mathrm{vo}}}{P_{at}}\right) - 0.15 \quad \text{where} \quad n \le 1 \tag{A.8}$$

The soil behavior type index I_c is defined by Wride [27] as

$$I_c = \sqrt{(3.47 - \log Q)^2 + (1.22 + \log F)^2} \tag{A.9}$$

where Q and F are the normalized tip resistance and friction ratio, respectively.

$$Q = \left(\frac{q_c - \sigma_{\mathrm{vo}}}{\sigma'_{\mathrm{vo}}}\right) \tag{A.10}$$

$$F = \left(\frac{f_s}{q_c - \sigma_{\mathrm{vo}}}\right) \times 100 \tag{A.11}$$

Once CSR and CRR are obtained, the factor of safety against liquefaction triggering at a particular depth z can be calculated

$$\mathrm{FS} = \frac{\mathrm{CRR}}{\mathrm{CSR}} \tag{A.12}$$

which is used to calculate the liquefaction potential index detailed in the following section.

Appendix B. Liquefaction potential index

Following the definition given in [4,30], LPI is usually evaluated for the top 20 m of soil profile as

$$\mathrm{LPI} = \int_0^{20} F_L w(z)dz \tag{B.13}$$

where z denotes the depth in meters and $w(z) = 10 - 0.5z$; F_L is defined as [31]

$$F_L = \begin{cases} 0 & \text{FS} \geq 1.2 \\ 1 - \text{FS} & \text{FS} \leq 0.95 \\ 2 \times 10^6 e^{-18.427\text{FS}} & 0.95 < \text{FS} < 1.2 \end{cases} \quad \text{(B.14)}$$

where FS is the factor of safety defined in (A.12) for CPT-based liquefaction evaluation. Herein, we adopt a discrete form of the integral to calculate LPI along the depth of a given soil profile [43,13]

$$\text{LPI} = \sum_{i=1}^{N} w_i F_{Li} H_i \quad \text{(B.15)}$$

where H_i is the thickness of the discrete layer and is determined by the CPT sampling frequency (H_i=0.1 m for this study); N is the number of soil layers.

References

[1] Kramer SL. Geotechnical earthquake engineering. Upper Saddle River, New Jersey: Prentice-Hall Inc; 1996.
[2] National Research Council (NRC) Committee on Earthquake Engineering Research. Liquefaction of soils during earthquakes. National Academies. 1985.
[3] T.L. Youd, I.M. Idriss, R.D. Andrus, I. Arango, G. Castro, J.T. Christian, et al. Liquefaction resistance of soils summary report from the 1996 NCEER and 1998 NCEER/NSF workshops on evaluation of liquefaction resistance of soils. J Geotech Geoenviron Eng. 2001, 127(4), p. 297–13.
[4] T. Iwasaki, F. Tatsuoka, K. Tokida, S. Yasuda, A practical method for assessing soil liquefaction potential based on case studies at various sites in Japan. In: Proceedings of the 2nd international conference on Microzonation. 1978, p. 885–96.
[5] DeGroot DJ, Baecher GB. Estimating autocovariance of in-situ soil properties. J Geotech Eng 1993;119(1):147–66.
[6] Goovaerts P. Geostatistics for natural resources evaluation. New York: Oxford University Press; 1997.
[7] Vanmarcke E. Random fields: analysis and synthesis. Singapore: World Scientific Publishing Co. Pte. Ltd; 2010.
[8] Popescu R, Prévost JH, Deodatis G. Effects of spatial variability on soil liquefaction: some design recommendations. Géotechnique 1997;47(5):1019–36.
[9] Fenton GA, Vanmarcke EH. Spatial variation in liquefaction risk. Géotechnique 1998;48(6):819–31.
[10] Elkateb T, Chalaturnyk R, Robertson PK. Simplified geostatistical analysis of earthquake-induced ground response at the Wildlife Site, California, USA. Can Geotech J 2003;40(1):16–35.
[11] Popescu R, Prevost JH, Deodatis G. 3D effects in seismic liquefaction of stochastically variable soil deposits. Géotechnique 2005;55(1):21–31.
[12] Liu CN, Chen CH. Mapping liquefaction potential considering spatial correlations of CPT measurements. J Geotech Geoenviron Eng 2006;132(9):1178–87.
[13] Lenz JA, Baise LG. Spatial variability of liquefaction potential in regional mapping using CPT and SPT data. Soil Dyn Earthq Eng 2007;27(7):690–702.
[14] Baker JW, Faber MH. Liquefaction risk assessment using geostatistics to account for soil spatial variability. J Geotech Geoenviron Eng 2008;134(1):14–23.
[15] Pokhrel RM, Kuwano J, Tachibana S. A kriging method of interpolation used to map liquefaction potential over alluvial ground. Eng Geol 2013;152(1):26–37.
[16] Vivek B, Raychowdhury P. Probabilistic and spatial liquefaction analysis using CPT data: a case study for alameda country site. Nat Hazards 2014;71(3):1715–32.
[17] Chen Q, Wang C, Juang CH. CPT-based evaluation of liquefaction potential accounting for soil spatial variability at multiple scales. J Geotech Geoenviron Eng 2015;04015077.
[18] Fenton GA. Random field modeling of cpt data. J Geotech Geoenviron Eng 1999;125(6):486–98.
[19] Uzielli M, Vannucchi G, Phoon KK. Random field characterisation of stress-nomalised cone penetration testing parameters. Géotechnique 2005;55(1):3–20.
[20] Holzer TL, Blair JL, Noce TE, Bennett MJ. Predicted liquefaction of East Bay fills during a repeat of the 1906 San Francisco earthquake. Earthq Spectra 2006;22(S2):261–77.
[21] Thomas HL, Michael BJ, Thomas NE, Padovani AC, Tinsley JC. III, Liquefaction hazard mapping with lpi in the greater oakland, california, area. Earthq Spectra 2006;22(3):693–708.
[22] Baise LG, Higgins RB, Brankman CM. Liquefaction hazard mapping - statistical and spatial characterization of susceptible units. J Geotech Geoenviron Eng 2006;132(6):705–15.
[23] Baise LG, Lenz JA, Thompson EM. Discussion of mapping liquefaction potential considering spatial correlations of CPT measurements by Chia-Nan Liu and Chien-Hsun Chen. J Geotech Geoenviron Eng 2008;134(2):262–3.
[24] Ballegooy S van, Wentz F, Boulanger RW. Evaluation of cpt-based liquefaction procedures at regional scale. Soil Dyn Earthq Eng 2015;79:315–34.
[25] Baker JW, Seifried A, Andrade JE, Chen Q. Characterization of random fields at multiple scales: an efficient conditional simulation procedure and applications in geomechanics. Appl Stat Probab Civ Eng 2011:347.
[26] Chen Q, Seifried A, Andrade JE, Baker JW. Characterization of random fields and their impact on the mechanics of geosystems at multiple scales. Int J Numer Anal Methods Geomech 2012;36(2):140–65.
[27] Robertson PK, Wride CE. Evaluating cyclic liquefaction potential using the cone penetration test. Can Geotech J 1998;35(3):442–59.
[28] Robertson PK. Performance based earthquake design using the CPT. Proc IS-Tokyo 2009:3–20.
[29] Ku CS, Juang CH, Chang CW, Ching J. Probabilistic version of the robertson and wride method for liquefaction evaluation: development and application. Can Geotech J 2011;49(1):27–44.
[30] T. Iwasaki, K. Tokida, F. Tatsuoka, S. Watanabe, S. Yasuda, H. Sato, Microzonation for soil liquefaction potential using simplified methods. In: Proceedings of the 3rd international conference on microzonation, Seattle, volume 3. 1982, p. 1310–30.
[31] Sonmez H. Modification of the liquefaction potential index and liquefaction susceptibility mapping for a liquefaction-prone area (Inegol, Turkey). Environ Geol 2003;44(7):862–71.
[32] Toprak S, Holzer TL. Liquefaction potential index: field assessment. J Geotech Geoenviron Eng 2003;129(4):315–22.
[33] Sonmez H, Gokceoglu C. A liquefaction severity index suggested for engineering practice. Environ Geol 2005;48(1):81–91.
[34] Juang CH, Liu CN, Chen CH, Hwang JH, Lu CC. Calibration of liquefaction potential index: a re-visit focusing on a new CPTU model. Eng Geol 2008;102(1):19–30.
[35] Maurer BW, Green RA, Cubrinovski M, Bradley BA. Assessment of cpt-based methods for liquefaction evaluation in a liquefaction potential index framework. Géotechnique 2015;65(5):328–36.
[36] Deutsch CV, Journel AG. GSLIB: geostatistical software library and user's guide. New York: Oxford University Press; 1992.
[37] Leuangthong O, Khan KD, Deutsch CV. Solved problems in geostatistics. Hoboken, New Jersey: John Wiley & Inc.; 2011.
[38] L.J. Brown, J.H. Weeber, Geology of the Christchurch Urban Area, Institute of Geological and Nuclear Sciences 1:25,000 Geological Map 1. 1992.
[39] B.A. Bradley, M. Hughes, Conditional peak ground accelerations in the canterbury earthquakes for conventional liquefaction assessment. In: Technical report for the ministry of business, innovation and employment, New Zealand. 2012.
[40] Khoshnevisan S, Juang H, Zhou YG, Gong W. Probabilistic assessment of liquefaction-induced lateral spreads using CPT focusing on the 2010–2011 Canterbury earthquake sequence. Eng Geol 2015;192:113–28.
[41] Cressie N. Fitting variogram models by weighted least squares. J Int Assoc Math Geol 1985;17(5):563–86.
[42] J. Beavan, S. Levick, J. Lee, K. Jones, Ground displacements and dilatational strains caused by the 2010–2011 canterbury earthquakes. GNS Science Consultancy Report. 67:59, 2012.
[43] Luna R, Frost JD. Spatial liquefaction analysis system. J Comput Civ Eng 1998;12(1):48–56.
[44] Liu W, Chen Q, Wang C, Juang CH, Chen G. Spatially correlated multiscale Vs30 mapping and a case study of the Suzhou site. Eng Geol 2017. http://dx.doi.org/10.1016/j.enggeo.2017.01.026.